

Titre: Investigation of submarine permafrost conditions in the Canadian Beaufort Sea using diving wave tomography

Auteurs: Henrik Grob, Dirk Klaeschen, Michael Riedel, Sebastian Krastel, Mathieu J. Duchesne, Jefferson Bustamante Restrepo, Gabriel Fabien-Ouellet, Young Keun Jin, & Jong Kuk Hong

Date: 2025

Type: Article de revue / Article

Référence: Grob, H., Klaeschen, D., Riedel, M., Krastel, S., Duchesne, M. J., Restrepo, J. B., Fabien-Ouellet, G., Jin, Y. K., & Hong, J. K. (2025). Investigation of submarine permafrost conditions in the Canadian Beaufort Sea using diving wave tomography. Journal of Geophysical Research: Solid Earth, 130(4), 18 pages.
Citation: <https://doi.org/10.1029/2024jb029955>

 **Document en libre accès dans PolyPublie**
Open Access document in PolyPublie

URL de PolyPublie: <https://publications.polymtl.ca/64479/>
PolyPublie URL:

Version: Version officielle de l'éditeur / Published version
Révisé par les pairs / Refereed

Conditions d'utilisation: Creative Commons Attribution 4.0 International (CC BY)
Terms of Use:

 **Document publié chez l'éditeur officiel**
Document issued by the official publisher

Titre de la revue: Journal of Geophysical Research: Solid Earth (vol. 130, no. 4)
Journal Title:

Maison d'édition: Wiley
Publisher:

URL officiel: <https://doi.org/10.1029/2024jb029955>
Official URL:

Mention légale: © 2025. The Author(s). This is an open access article under the terms of the Creative Commons Attribution License (<http://creativecommons.org/licenses/by/4.0/>), which permits use, distribution and reproduction in any medium, provided the original work is properly cited.
Legal notice:

JGR Solid Earth

RESEARCH ARTICLE

10.1029/2024JB029955

Key Points:

- Application of a diving wave tomography to infer present submarine permafrost conditions on the southern Canadian Beaufort Shelf
- Heterogeneous permafrost conditions show permafrost thawing in the outer ~27 km of the shelf
- Seismic anisotropy in ice-bearing sediments complicates ice state and content quantification

Supporting Information:

Supporting Information may be found in the online version of this article.

Correspondence to:

H. Grob,
henrik.grob@ifg.uni-kiel.de

Citation:

Grob, H., Klaeschen, D., Riedel, M., Krastel, S., Duchesne, M. J., Bustamante, J., et al. (2025). Investigation of submarine permafrost conditions in the Canadian Beaufort Sea using diving wave tomography. *Journal of Geophysical Research: Solid Earth*, 130, e2024JB029955. <https://doi.org/10.1029/2024JB029955>

Received 24 JUL 2024

Accepted 3 APR 2025







Author Contributions:

Conceptualization: H. Grob, M. Riedel
Data curation: Y. K. Jin, J. K. Hong
Formal analysis: H. Grob, D. Klaeschen
Funding acquisition: M. Riedel, S. Krastel
Investigation: H. Grob, M. Riedel
Methodology: D. Klaeschen, M. Riedel
Project administration: M. Riedel, S. Krastel, Y. K. Jin, J. K. Hong
Supervision: M. Riedel, S. Krastel, M. J. Duchesne
Validation: D. Klaeschen
Visualization: H. Grob
Writing – original draft: H. Grob
Writing – review & editing: H. Grob, D. Klaeschen, M. Riedel, S. Krastel,

© 2025. The Author(s).

This is an open access article under the terms of the [Creative Commons Attribution License](#), which permits use, distribution and reproduction in any medium, provided the original work is properly cited.

Investigation of Submarine Permafrost Conditions in the Canadian Beaufort Sea Using Diving Wave Tomography

H. Grob¹ , D. Klaeschen², M. Riedel² , S. Krastel¹ , M. J. Duchesne³, J. Bustamante³ , G. Fabien-Ouellet⁴ , Y. K. Jin⁵ , and J. K. Hong⁵ 

¹Kiel University, Kiel, Germany, ²GEOMAR Helmholtz Centre for Ocean Research Kiel, Kiel, Germany, ³Geological Survey of Canada, Quebec, QC, Canada, ⁴Polytechnique Montreal, Montreal, QC, Canada, ⁵Korea Polar Research Institute, Incheon, Republic of Korea

Abstract Submarine permafrost in the Canadian Beaufort Sea is relict terrestrial permafrost, which is continuously degrading since the change of thermal conditions induced by a marine transgression that followed the last glaciation. Permafrost degradation has a crucial socio-ecological significance because its thawing can result in geohazards like landslides or an increase in greenhouse gas emissions. These consequences are mostly regulated by the state of ice in permafrost. In this study, we use marine multichannel seismic data to apply a diving wave tomographic inversion on the outer 50 km of the Canadian Beaufort Shelf. Due to the close relationship between seismic velocity and ice content, we are able to infer detailed information about the present submarine permafrost condition. We find a clear variability of permafrost occurrences between the inner and outer Canadian Beaufort Shelf. At the inner shelf, discontinuous ice-bonding permafrost occurs extensively close to the seafloor but is interrupted by taliks. Within the outer ~27 km of the shelf, ice-bonding permafrost is absent in the upper sediments and its top has plunged to >200 m below sea level. These findings add new details to the current state of the degrading permafrost. In addition, we observe seismic anisotropy in the frozen permafrost sediments.

Plain Language Summary The southern Canadian Beaufort Shelf contains submarine permafrost, ground below the seafloor that remains perennially below 0°C. Over the last ~1 million years, permafrost formed in the ground as the continental shelf was exposed to cold Arctic air. With the end of the last glaciation, the sea level rose and flooded the continental shelf with warmer water causing the still ongoing thawing of permafrost. Permafrost is an important climate variable because its thawing can cause the release of greenhouse gases and poses a geohazard in form of landslides and ground collapses. These consequences are mostly regulated by the state and content of ice in permafrost. In this work, we investigate the submarine permafrost conditions on the Canadian Beaufort Shelf using a seismic inversion method. By applying a diving wave tomography, we can derive seismic velocities in the subsurface that are linked to the state and content of ice. We find that ice-bonding permafrost has already been thawed in the upper sediments of the outer ~27 km of the shelf and observe seismic anisotropy in the frozen sediments. This work adds new details to the current state of permafrost thawing on the Canadian Beaufort Shelf.

1. Introduction

Permafrost is defined as ground that remains below 0°C for at least two consecutive years and in the presence of ice, permafrost is referred to be frozen or ice-bearing (e.g., Dobinski, 2011; Osterkamp, 2001; van Everdingen, 1998). Submarine permafrost beneath much of the Arctic shelf is less studied than terrestrial permafrost and is reckoned as widely unexplored (Angelopoulos et al., 2020). In the perspective of climate change, submarine permafrost has a socio-ecological significance because its thawing could accelerate global warming and poses a geohazard in form of landslides and ground collapses (e.g., Angelopoulos et al., 2020; Natali et al., 2021; Ruppel & Kessler, 2017; Schuur et al., 2015). Thawing of permafrost may destabilize intra-permafrost gas hydrates, release previously trapped free gas and subject the organic carbon to enhanced microbial decomposition, increasing significantly greenhouse gas emissions (Ruppel & Kessler, 2017; Wild et al., 2022). These processes are mostly regulated by the ice content of the permafrost and further amplify the climate feedback of thawing permafrost (Schuur et al., 2022). Evidence for these processes was shown, for example, by Shakhova et al. (2017) in the East Siberian Arctic Shelf region, where submarine permafrost is thawing more rapidly than terrestrial permafrost. In addition, Wild et al. (2022) noted that the thawing of submarine permafrost in that region may contribute to increased ocean acidification.

M. J. Duchesne, J. Bustamante, G. Fabien-Ouellet, Y. K. Jin, J. K. Hong

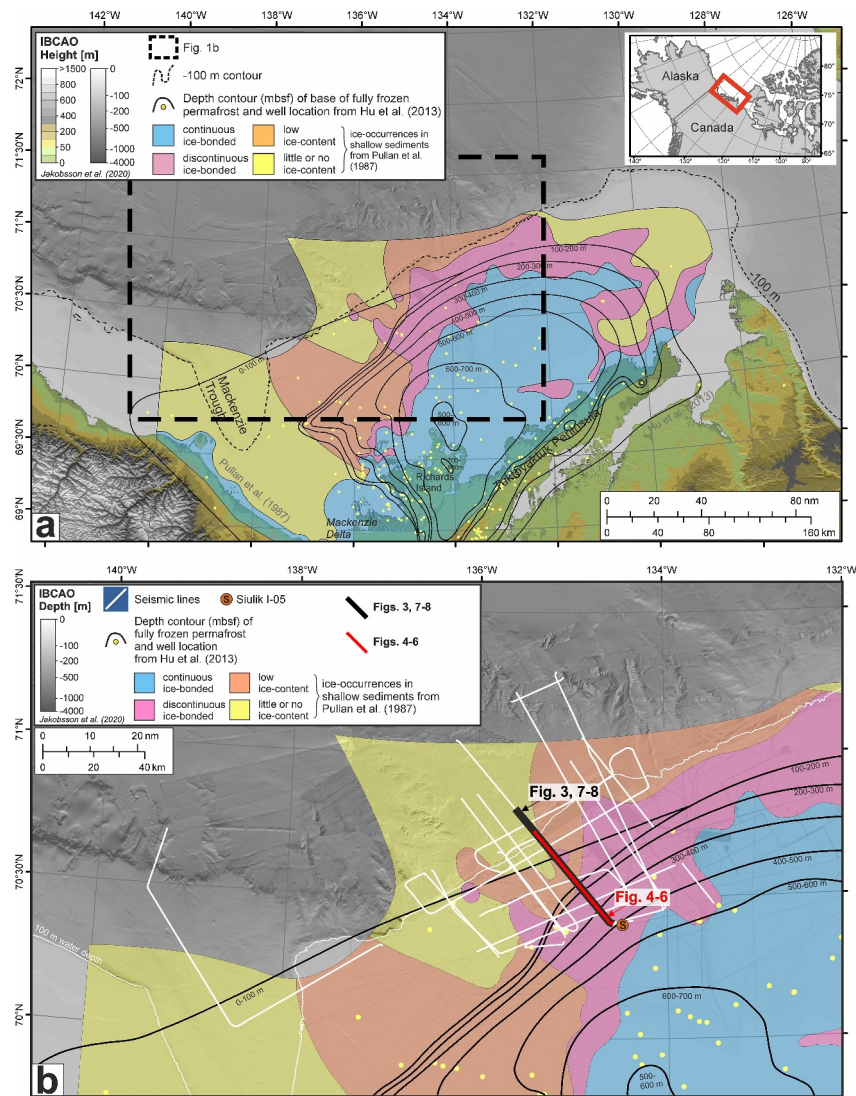


Figure 1. Overview map of the Canadian Arctic Beaufort Sea. In (a) ice-occurrences in shallow sediments analyzed by seismic refractions (Pullan et al., 1987) as well as the depth of the base of fully frozen permafrost based on well data (Hu et al., 2013) are shown. (b) Shows a close-up of the study area with the location of the seismic data set. The red line indicates the part of the seismic line used for the diving wave tomography, the black line illustrates the extent used for the prestack depth migration. The maps are projected in UTM8N. Bathymetry data are taken from the International Bathymetric Chart of the Arctic Ocean (IBCAO) (Jakobsson et al., 2020) and in the region of the slope by courtesy of industry, GSC, and the Canadian university consortium ArcticNet (Blasco et al., 2013).

1.1. Evolution of Submarine Permafrost in the Arctic

The Canadian Arctic Beaufort Sea is located on the northwest coast of the Yukon and the Northwest Territories in Canada, close to the Canada-U.S. border (Figure 1). It is characterized by a shallow, large continental shelf that transitions into the continental slope at 80–120 m water depth (Carmack et al., 1989; Dixon & Dietrich, 1990).

Most of the present submarine permafrost in the Arctic is relict terrestrial permafrost and occurs under the circum-Arctic continental shelf regions of the seas of Siberia, Chukchi and U.S. and Canadian Beaufort Sea (Angelopoulos et al., 2020; Overduin et al., 2019). Beginning as early as the end of the Pliocene, thermal conditions during glacial periods favored the formation of permafrost and gas hydrates whereas interglacial periods led to their thawing and destabilization (Lewis & Collett, 2013). After the last glacial maximum ~25 kaBP(cal), an ongoing marine transgression inundated Arctic Shelf areas and the sea level rose by ~120 m (Peltier & Fairbanks, 2006), which changed their environmental setting from subaerial to submarine. The inundation led to warming from

former air temperatures of $<-20^{\circ}\text{C}$ to present bottom water temperatures of $\sim-1^{\circ}\text{C}$ (Brigham & Miller, 1983; Taylor et al., 2013). In the Canadian Beaufort Sea, the coldest waters are found today below the seasonal thermocline between ~ 30 and 200 m water depth with mean annual temperatures of $<-1^{\circ}\text{C}$ and maximum temperatures are found at ~ 350 m at 0.5°C (Carmack et al., 1989; McLaughlin et al., 2004). Since the end of the last glaciation, the relict offshore permafrost is degrading and still reacting to the thermal change due to slow rates of heat diffusion and latent heat effects associated with thawing (Jin et al., 2015; Riedel et al., 2017; Taylor et al., 1996). Even in the presence of negative seabed temperatures, submarine ice-bearing permafrost (IBPF) can thaw by the intrusion of saline oceanic water because salt depresses the freezing point of the pore water (Osterkamp, 2001). Saline frozen soils are widespread on the Arctic coast (Brouchkov, 2003). Hivon and Sego (1993) found onshore saline permafrost in the Northwest Territories and along the Canadian Beaufort Sea coast. King et al. (1982) reported saline submarine permafrost samples in the offshore Beaufort Sea.

1.2. Submarine Permafrost in the Canadian Beaufort Sea

Since the Holocene marine transgression, the present seaward extent of the >500 m thick relict permafrost body in the Canadian Beaufort Sea has retreated by ~ 2 km and is assumed to be located <2 km off the shelf edge around the 100 m isobath (Taylor et al., 2013; compare Figure 2a). Analysis of seismic refraction data by Pullan et al. (1987) showed that the submarine IBPF is concentrated in the central shelf and it is decreasing radially but extends more to the northeast (Figure 1a). Analysis of industry borehole data by Hu et al. (2013) further showed that the depth of the base of the fully frozen permafrost is distributed with a maximum depth of >700 m that becomes radially shallower but also extends more towards the northeast. More knowledge about the submarine permafrost condition was obtained by numerical models along the Beaufort Shelf (Frederick & Buffett, 2015; Taylor et al., 2013). Those works proposed a wedge-like shape of the present permafrost body thinning out close to the shelf margin. The permafrost base seemed to be raised by ~ 100 m since the Last Glacial Maximum and a present seaward extent of the submarine permafrost may be at 134°W at the ~ 95 m isobath. Despite the intensive scientific research for >40 years and offshore exploration for hydrocarbons in the 1980s and 1990s in the southern Canadian Beaufort Sea (e.g., Dallimore et al., 2015; Dixon, 1996), more research on the present extent of submarine permafrost beneath the continental shelf, especially near the seafloor, is required because this region is one of the most vulnerable to ongoing global warming.

1.3. Geophysical Methods for Submarine Permafrost Investigation

Investigation methods for submarine IBPF generally comprise borehole and core logging, pore ice and fluid sampling, electrical surveys and different types of seismic measurement (Angelopoulos et al., 2020; Gwiazda et al., 2018; Paull et al., 2011). The latter two represent the main methods to remotely investigate and map submarine IBPF, which exploit the unique acoustic and electrical properties of permafrost in the presence of ice (Duchesne et al., 2022). For instance, Sherman et al. (2017) and Sherman and Constable (2018) used controlled-source electromagnetic surveys to map the submarine IBPF extent on the Alaskan Beaufort Shelf. They found significant lateral variability in the presence of IBPF and that IBPF may be preserved by fresh groundwater outflow.

Mapping submarine IBPF by seismic data utilizes the increase of seismic velocity with increasing ice content and includes seismic refraction analysis (e.g., Brothers et al., 2012; Hatlelid & MacDonald, 1982; Hunter et al., 1978; MacAulay & Hunter, 1982; Pullan et al., 1987), analysis of stacking velocities (Brothers et al., 2016), tomographic inversions (Kang et al., 2021; Ramachandran et al., 2011), the interpretation of seismic reflection data (Grob et al., 2023; Hinz et al., 1998; Matson et al., 2013; O'Connor et al., 1987; Portnov et al., 2013; Rekant et al., 2015), or ambient noise analyses (Overduin et al., 2015).

The detection and mapping of submarine IBPF is challenging because the shallow marine setting of the continental shelves in combination with strong acoustic impedance contrasts of water, unfrozen sediments and IBPF cause high-energy free surface multiples, which overprint primary signals (Duchesne et al., 2022). While on land, the ground is frozen from the surface down to the base of IBPF creating a sharp impedance contrast, submarine IBPF is generally sandwiched between unfrozen layers above and beneath. These shallow heterogeneities cause significant changes in seismic velocities creating a seismically complex shallow subsurface.

An application of diving wave tomography (DWT) may overcome these challenges in submarine IBPF mapping associated with shallow pronounced velocity variations. The DWT is an inversion method for near-surface

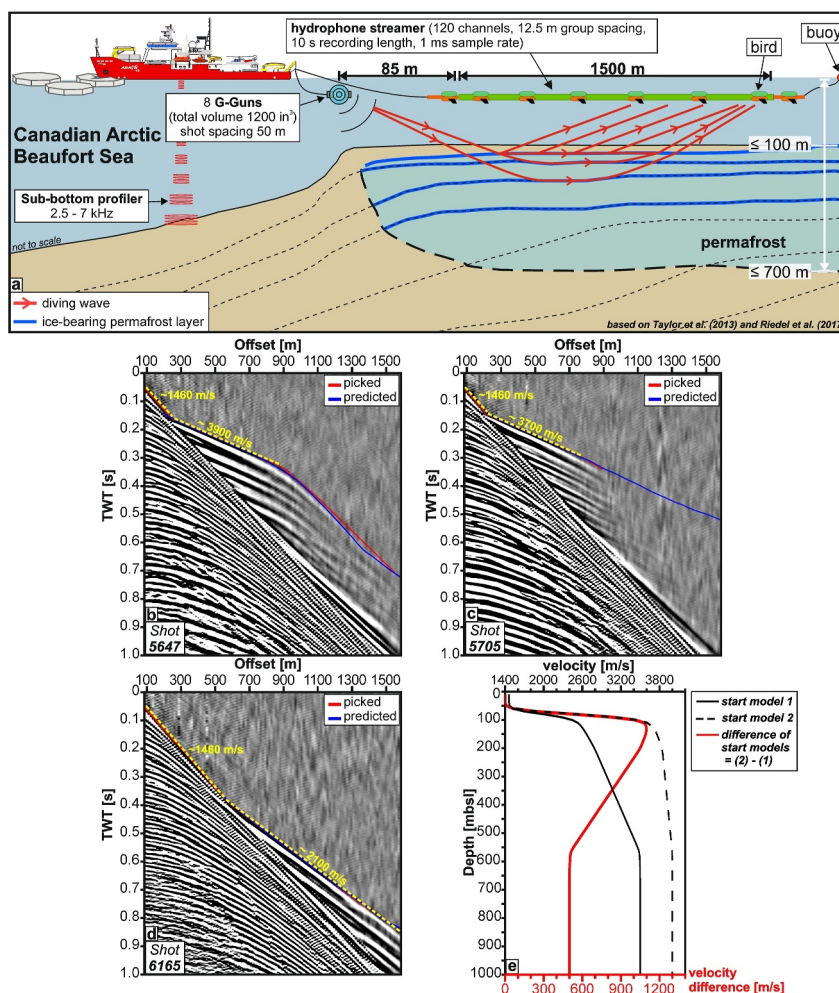


Figure 2. In (a), the sketch summarizes the acquisition geometry and the concept of diving waves propagating along ice-bearing permafrost layers. Shot gathers along line ARA05C-05 are shown in (b)–(d). Their locations are annotated in Figures 3 and 4. In (b)–(d), red lines illustrate manually picked travel times and blue lines show the travel times predicted by the diving wave tomography. Yellow dashed lines illustrate the rough manual linear moveout analyses and their velocity estimations. In (e), the mean 1D velocity functions for two 2D start models as well as their difference are shown in meters below sea level (mbsl).

velocity model estimation. Therefore, it is well suited to generate reliable velocity models in the presence of a complex shallow subsurface concomitant with pronounced velocity variations (Stefani, 1995; Tanis et al., 2006). While in the case of head waves the propagating waves get refracted at discrete layer interfaces with constant velocity, diving waves (or turning rays) occur where positive velocity gradients exist (see Figure 2a). In the case of a velocity gradient, which can be a result for example, of progressive compaction effects or existing IBPF with variable ice saturations, the propagating waves become continuously refracted and thereby “turned” (Kearey et al., 2002). In the presence of a continuously increasing velocity with depth, diving waves travel along a curved ray path and after passing a turning point at some depth may return to the surface (Kearey et al., 2002; Zhu et al., 1992).

1.4. Objectives

Due to the close relationship between seismic velocity and ice content, a detailed velocity model can be used to explore changes in conditions and the extent of submarine IBPF. In general, this can add information required for hazard investigations of offshore drilling or infrastructure projects, estimation of regional geohazards, as well as an assessment of permafrost degradation.

In this study, we investigate the application of a DWT onto a seismic line in a submarine permafrost environment to estimate the velocity distribution of the shallow subsurface. The seismic line is located on the outer ~48 km of the Canadian Beaufort Shelf where the transgressive warming has affected the permafrost for the longest time and thus, where its effects are likely to be most pronounced. The DWT velocity model allows a qualitative analysis along the seismic line of where submarine IBPF occurs. We are also investigating where IBPF has already thawed and how deep the top of IBPF has sunk. While the DWT is laterally and vertically high in resolution, the investigations depend on the actual maximum depth reached by the diving waves. In addition, the DWT velocity field serves as a key component to build a complete velocity model that allows an optimized depth migration and improved imaging at depth when submarine IBPF is present.

2. Acoustic Properties of Ice-Bearing Permafrost

DWT not only provides an image of the subsurface velocity distribution, it also allows these velocities to be quantified. However, it is not possible to quantify the accurate ice content from seismic velocity alone. In this section, we explain what factors are the most important and how they affect the acoustic properties of IBPF. Understanding these properties is key to infer the IBPF's condition.

Permafrost conditions are distinguished by the content of frozen and unfrozen water. Permafrost that does not contain any water is called dry. Wet permafrost in contrast only contains liquid water, and frozen or IBPF contains ice in the pore spaces (Dobinski, 2011; Osterkamp, 2001). Transitions between those different permafrost conditions are fluent. The relative proportion of sediment, ice, pore fluid and pore gas determines the acoustic properties of the permafrost, in which changes in ice content are most significant (Dou et al., 2016). Temperature changes have large effects on seismic properties because physical properties of ice and unfrozen pore fluids are strongly temperature dependent. Other factors that affect ice-freezing or ice-thawing process are the mineral composition of the sediment matrix, grain size, texture, pore-water chemistry, and stress forces (Hu et al., 2013; King et al., 1988).

Processes affecting the ice content have a crucial impact on seismic properties. P-wave velocities of IBPF ground generally increase with increasing ice content (e.g., Dou et al., 2016; Johansen et al., 2003; King et al., 1988; Matsushima et al., 2016; Zimmerman & King, 1986). For example, frozen silt can have similar P-wave velocities as unfrozen sand (King et al., 1982) or moreover, frozen unconsolidated sediments can exhibit velocities in the range of unfrozen consolidated sedimentary rocks (Pullan et al., 1987).

Pore water salinity has a significant effect on the P-wave velocity of IBPF (Dou et al., 2016). Saline IBPF can thaw at sub-zero temperatures due to a freezing-point depression by the dissolved salts. Already 1/6 of the typical seawater salinity can reduce the P-wave velocities up to 12%–36% compared to non-saline IBPF in the temperature range from -15 to -1°C (Dou et al., 2016). For instance, King et al. (1982) analyzed sediment samples from the Beaufort Shelf with different grain sizes and salinities. For temperatures of -1°C to -9°C , the authors noted velocity ranges for an offshore clay sample from $\sim 1,700$ to $2,500$ m/s with pore-water salinity of 0.3 M (~ 17 psu), for a silt sample from $\sim 2,100$ – $3,600$ m/s with 0.13 M (~ 7.6 psu) and for a sand sample $\sim 3,200$ – $4,000$ m/s with 0.02 – 0.08 M (~ 1 – 4.6 psu).

Physical properties of IBPF ground also depend upon how the ice grows (Dou et al., 2016). When ice grows at the grain surfaces, the ice can cement the grains either by having contact with the grain or by coating the grains. The cementing ice distribution results in an increase in frame stiffness and IBPF becomes ice-bonded showing a steep increase of seismic velocity already at low ice saturations. Johansen et al. (2003) denote a theoretical step velocity increase that possibly shows the onset of ice-bonding. In fully water-saturated sediments, the velocity increased from $2,500$ to $2,800$ m/s for 0% – 40% ice fraction to $3,500$ – $4,300$ m/s for 40% – 100% ice fraction.

Alternatively, the ice may grow within the pore fluid and the ice distributes as pore-filling. The resulting increase of seismic velocities is not as pronounced as for the ice-bonding due to a smaller effect on the frame stiffness (Dou et al., 2016; Schindler et al., 2016). However, Dou et al. (2016) proposed a combination of diverse pore ice distributions because neither a pure cementing nor a pure pore filling distribution could explain their velocity measurements.

In consequence, an interpretation of the detailed condition of IBPF only based on seismic velocities is limited due to the variety of factors affecting the seismic velocities. Appropriate knowledge of the geological and geochemical properties of the subsurface would be required to map ice saturations quantitatively. This means that

a combination of seismic data with electrical resistivity and drilling (core) data is required. None of these methods alone are thus appropriate to quantify detailed ice conditions.

At the same time, the pronounced dependence on ice content and seismic velocity provides a possibility to distinguish qualitatively frozen from unfrozen permafrost. For example, in the Mackenzie Delta and the surrounding Beaufort Sea, Hatlelid and MacDonald (1982) linked velocities of 1,524–1,981 m/s to unfrozen sediments and velocities of 2,438–4,267 m/s to frozen sediments. Moreover, Pullan et al. (1987) used velocities of 1,800–4,500 m/s for their interpretation of shallow ice-bonded frozen material on the Canadian Beaufort Shelf, and at the U.S. Beaufort shelf, Brothers et al. (2012) inferred IBPF layers from refractions with velocities >2,300 m/s. Finally, as previously mentioned, King et al. (1982) investigated a velocity range of ~1,700–4,000 m/s for different frozen sediment samples from the Beaufort Shelf.

3. Data and Methods

3.1. Data

In this study, we investigate the ability of a DWT to provide a more detailed submarine IBPF distribution. We apply the DWT to seismic line five of expedition ARA05C conducted with the research icebreaker ARAON operated by Korea Polar Research Institute (KOPRI) in 2014 which is representative of the general Canadian Beaufort Shelf setting (Jin & Dallimore, 2016). The line runs from the inner shelf in the southeast crossing the shelf edge towards the continental slope in the northwest (Figure 1b).

The seismic system used during ARA05C consisted of an airgun array and a multichannel streamer (Figure 2a). The air gun array consisted of 8 G-Guns with a total volume of 1,200 in³ (~20 l). The array was fired every 50 m. The streamer had a length of 1.5 km with 120 channels at a channel group spacing of 12.5 m. The streamer was towed 85 m behind the air gun array (minimum offset). The data were recorded for 10 s and sampled at 1 ms (Jin & Dallimore, 2016). In the upper ~0.5 s TWT, the data quality is affected by a reduced number of traces recording reflected energy necessary for NMO velocity analysis and stacking, significant NMO stretch effects due to shallow high subsurface velocity contrasts and high-energy free-surface multiples masking primary signals.

In preparation for the application of the DWT, the pre-processing was set to a minimum and only a 4 Hz low-cut frequency filter was applied to the shot gathers. Both the 4 Hz low-cut filter and the subsequent DWT were applied in Schlumberger's OMEGA Geophysical Data Processing Platform. In addition, we present sub-bottom profiler (SBP) data of a Kongsberg SBP 120 system that operated in a frequency range between 2.5–7 kHz with a system beam width of 12° (Jin & Dallimore, 2016).

3.2. Diving Wave Tomography (DWT)

The DWT algorithm implemented in the software OMEGA2 from Schlumberger is a non-linear ray-tracing inversion algorithm that solves the eikonal equation based on Podvin and Lecomte (1991). The algorithm is solved iteratively, which includes first-break picking, ray tracing performing, calculation of time difference between observed and predicted travel times and the setup of linear equations. The system of linear equations is set by the ray path distances and time differences within each cell to find slowness perturbations. The differences between observed and predicted travel times are minimized based on a least squares method by Paige and Saunders (1982) and the velocity model is updated iteratively.

As initial step, first breaks were picked for 936 shots as long as refractions/diving waves were identifiable (e.g., Figures 2b–2d, Figure S2 in Supporting Information S1). No refractions were recorded for water depths >~110 m. As can be seen in Figures 2b–2d by the red lines, we picked the first breaks as gradual events because first breaks need not be linear in the case of diving waves (Abdul Basit et al., 2022). We built a start velocity model that was based on depth-velocity pairs we inferred from a rough manual linear moveout velocity analysis assuming horizontal interfaces. The underlying mean velocity function of the start model is shown in Figure 2e. To ensure convergence during inversion, the start velocity model used slightly slower velocities than the highest velocities observed.

We calculated the P-wave model over a total of 60 iterations to a maximum depth of 1.5 km with a vertical cell-size of 10 m and a total horizontal length of ~48 km. The horizontal cell size was set to 50 m and after 30 iterations, it was reduced to a final cell size of 25 m. The small cell size was required to account for very localized

changes in the velocity field. We constrained the valid velocity range for the eikonal solver to 1,460–6,000 m/s and adjusted every sixth iteration the damping parameter and the time error threshold of the Least Squares Solver to ensure convergence and velocity refinement.

As a final step of each iteration, after updating the velocity model, smoothing was applied to the velocity model using increasing horizontal and vertical smoothing lengths with depth. The theoretical best resolution is equal to the cell size, 25 m in horizontal and 10 m in vertical direction.

3.3. Performance of the DWT

The OMEGA software provides different parameters to monitor the performance and convergence of the tomography. These parameters comprise estimations of errors for the difference between picked and predicted data, the percent change of the velocity field between iterations, and the number of returned rays (see Figure S1 in Supporting Information S1). We conducted parameter tests to achieve convergence and minimum errors without a reduction of the number of returned rays. The convergence was defined when the percent change did not vary any longer without reduction in the estimated error. In the end, the visual difference between picked and predicted travel times (compare Figures 2b–2d, Figure S2 in Supporting Information S1) served as the latest assessment of a result.

During all inversion runs, all parameters show an abrupt change after 30 iterations when the horizontal cell size was reduced. The initial and estimated errors decline with proceeding iterations. The percent change converges to <4% in the final iterations and the number of returned rays remains relatively constant.

4. Results

4.1. Result of Reflection Imaging

To provide a structural insight into the subsurface along line 5, the result of conventional seismic reflection processing of the upper 2 s is shown in Figure 3. The processing flow applied to the data is summarized in Supporting Information S1 and includes bandpass filtering, predictive deconvolution in tau-p domain, surface-related multiple elimination (SRME), NMO correction, stacking and finite-difference migration (Figure S3a in Supporting Information S1). This southeast-northwest running line is characterized by the shallow seafloor of the Canadian Beaufort Shelf, which begins to descend to the northwest at ~46 km distance and transitions to the continental slope. Based on Dixon et al. (1992), the shelf is underlain by >4,000 m thick sediments of the Pliocene to Pleistocene Iperk Sequence, which is seismically characterized by northwest prograding foreset reflections and overlying topset reflections (Figure 3, yellow dashed lines). The inflexion points of the dipping foreset reflections move upwards towards the continental slope. In general, the sequence in the mid- and outer-shelf areas consists of a basal interval of interbedded sandstone and shale overlain by a clay- and silt-dominant interval that, in turn, is overlain by sandstone. These lithological assemblages correspond to the bottomset, foreset and topset sediments, respectively (Dixon et al., 1992).

4.2. Result of the DWT

In the following, the term velocity refers to the interval velocity. The starting velocity model for the initial inversion iteration is shown in Figure 4a. As described above and shown in Figure 2e, the starting velocity model follows a gradient from the seafloor. This gradient was introduced because an unfrozen uppermost layer is observed as an uppermost high-amplitude reflection in the seismic data (Figure 3) coinciding with a loss of acoustic penetration in the SBP data (Figure 6a) which was interpreted as the top of IBPF by Grob et al. (2023). The gradient was then estimated by linear moveout velocities (cf. yellow dashed lines in Figures 2b–2d). The water velocity is 1,460 m/s above the start of the gradient function. From the seafloor to 30 m below the seafloor (mbsf) the seismic velocity increase from 1,600 m/s to 2,600 m/s and finally to 3,500 m/s for depths >500 mbsf.

The final tomography result (referred to as result 1) is illustrated for the upper 0.7 km depth in Figure 4b. Most velocity variations are encountered in the upper 300 m. In general, the velocity is increasing with depth besides shallow velocity inversions where high velocity layers overlay lower velocity layers. These velocity inversions occur more often in the first 20 km distance along the line in the southeast region but are also encountered again near the shelf edge in the northwest. For depths >350 m, the velocities seem to approach a constant velocity of 3,500 m/s with only very minor velocity changes. From <20 km distance along the profile, velocities increase to

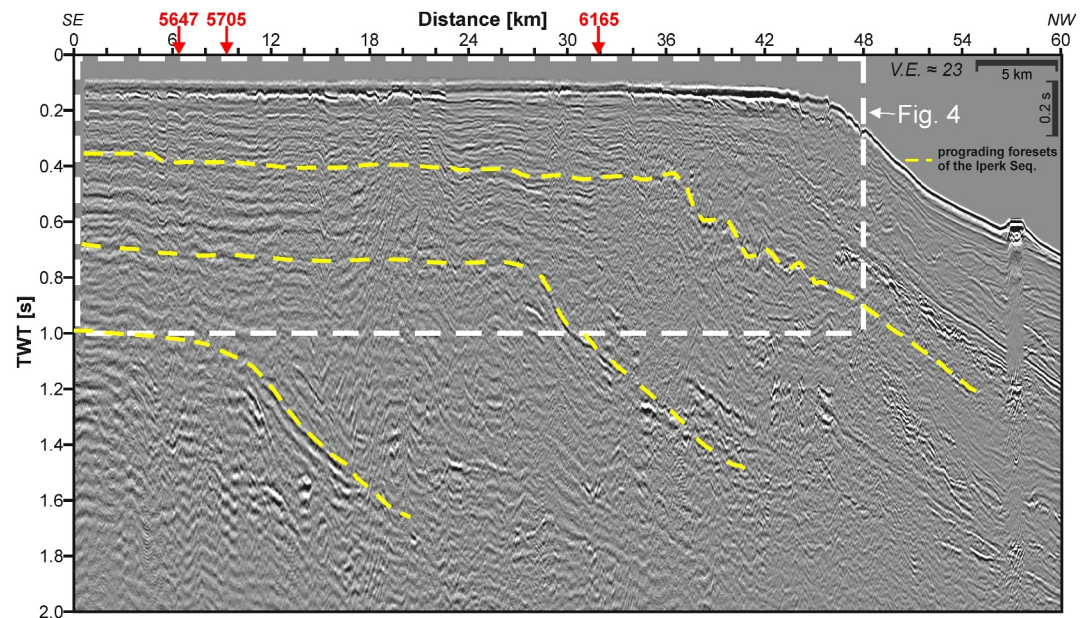


Figure 3. Seismic line 5 from expedition ARA05C. The locations of the shot gathers (shown in Figure 2) are marked by red arrows. Yellow dashed lines indicate the prograding foresets of the Iperk Sequence. The white dashed box shows the approximate extent of Figure 4. V.E. = vertical exaggeration.

values $\geq 2,450$ m/s within the upper 100 m. There, several vertical low-velocity zones incise into the predominantly high velocities within the upper 200 m. A major low-velocity zone exists between line distance 4.5–6.2 km. In contrast, from 20 km distance onward towards the slope region, velocities stay below 2,450 m/s within the upper 300 m.

5. Interpretation

5.1. Estimating the Depth of Reliable Velocities

Figure 5a shows the vertical velocity gradient of the final velocity model (result 1, Figure 4b). In general, starting at the seafloor, a high positive velocity gradient is observed with a thickness of ~ 30 m due to a significant velocity increase in areas where high velocity refracted events are observed, but which is locally interrupted in areas where no high velocity refractions were identified. This 30 m vertical gradient at the seafloor is an artefact of the gradient calculation on a 10 m vertical cell-size using a 5-point operator where the jump from water velocity to high/ice-bearing velocities is pronounced. Directly below this high velocity gradient at the seafloor negative gradients are observed which gradually change back again to a positive gradient at a depth of ~ 200 m. Only between ~ 22.5 –35 km distance, the gradient is more moderate and remains entirely positive. For depths > 300 m throughout the profile, the velocity gradient remains positive until it decreases to zero for depths > 600 m. In Figure 5b, the gradient of the start velocity function depicts major velocity changes in the upper 200 m, a slight velocity increase at 200–600 m and no changes for depths > 600 m.

We use the vertical gradient in Figure 5a to evaluate the coverage or maximum reliable depth of the tomographic inversion. We estimate the maximum depth of reliable velocities where the gradient becomes positive again, that is, where the velocities increase once more (black line in Figure 5c). In other words, the reliable depth limit is interpreted as the shallowest depth where the velocity gradient changes from negative to positive representing the depth at which the final model falls back to the start model. In particular, there is no indication in the data for a second positive gradient such as any second high-velocity event following the first refracted event that could cause a deep, positive gradient other than the start model. As the start model does not contain any negative gradient (Figure 4a), resulting negative gradients in the final velocity field cannot originate from the start model itself, meaning that the tomography must have affected this area. However, final velocities higher than start velocities can lead to negative gradients when the velocities approach or fall back to the start model.

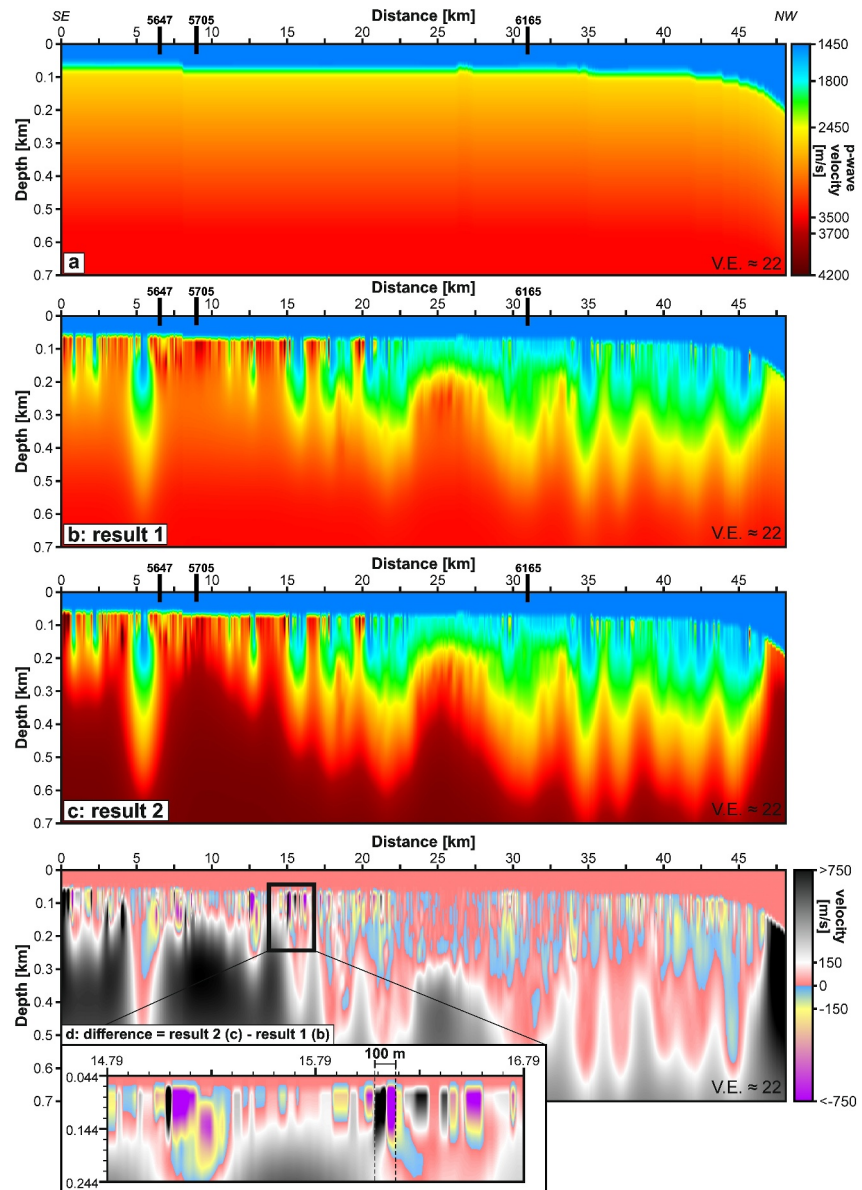


Figure 4. (a) Start velocity model 1 and (b) final velocity model 1 (result 1) after 60 iterations of the DWT. The final cell size is 25 m in horizontal and 10 m in vertical direction. (c) Final velocity model 2 (result 2) using higher start velocities (start velocity model 2, see Figure 2e). In (d), the difference between result 2 and result 1 is shown. The initial difference of the start velocity functions is illustrated in Figure 2e.

Therefore, the depth limit in Figure 5c is based on the vertical velocity gradient. As the velocities are very heterogeneous, we do not always find a clear transition from negative to positive gradients, such as between 22.5–35 km (compare shot gathers in Figure S2 in Supporting Information S1). There, the depth limit was manually estimated by a linear move out analysis of individual refracted arrivals (dashed line and question marks).

5.2. Interpretation of the Tomography Result

In the following section, we will use the term “talik” that describes unfrozen ground (i.e., neither ice-bearing nor ice-bonding) in permafrost (van Everdingen, 1998). The terms “inner” and “outer shelf” refer to a distance of <20 and >20 km, respectively. The interpretation of the velocity field is focused on velocities that may indicate ice-bonding permafrost (IBoPF). Corresponding to Duchesne et al. (2022), we interpret P-wave velocities lower than 2,450 m/s as non-ice-bonding, which is based on works by Dou et al. (2016), King et al. (1982), Matsushima

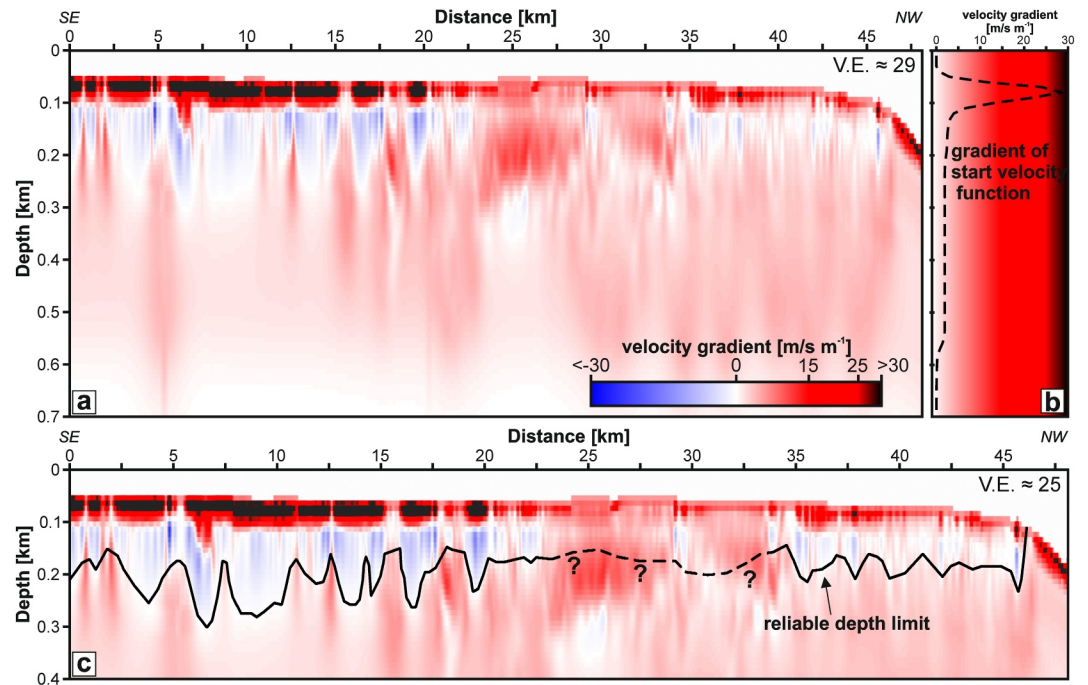


Figure 5. Vertical gradient of the final model 1 (result 1) and estimation of the reliable depth limit. A positive velocity gradient reflects increasing velocities in the final model and a negative velocity gradient decreasing velocities, respectively. Panel (a) shows the vertical gradient for 0.7 km depth along the profile, (b) the vertical gradient of start model 1 and (c) shows the upper 400 m with an estimated depth limit of reliable velocities. We pick the maximum depth of reliable velocities; that is, where the velocities increase again after a previous decrease. Between 22.5–35 km, this depth was estimated manually (dashed line and question marks). Note that the 30 m deep vertical gradient at the seafloor in (a) and (c) is an artefact of the gradient calculation on a 10 m vertical cell-size with a 5-point operator where the jump from water velocity to high/ice-bearing velocities is pronounced.

et al. (2016) and Zimmerman and King (1986). Velocities above 3,500 m/s are interpreted as well-bonding; velocities between 2,450 and 3,500 m/s as partially ice-bonding (Figure 6). In partially-bonded permafrost, only parts of the soil particles are held together by ice, whereas in well-bonded permafrost, all soil particles are strongly cemented together by ice (van Everdingen, 1998).

The occurrence of IBoPF (both partially- and well-bonding) shows a clear trend with increasing distance towards the shelf edge (Figure 6). For the first 15 km distance along the profile, the IBoPF at the near-surface occurs extensively discontinuous (i.e., 65%–90% of the area underlain by permafrost after Pelletier & Medioli, 2014), but decreases abruptly to intermediate discontinuous (36%–65%) for the subsequent 5 km and is basically absent for the remainder of the line towards the shelf edge. While, at the inner shelf, the top of IBoPF is mainly located right beneath the seafloor, the undulating top of IBoPF plunges up to a maximum depth of almost 400 m towards the shelf edge—deeper than the estimated reliable depth (Figure 6b). Only isolated ice lenses are encountered locally at the near-surface that have no contact with the top of IBoPF at the outer shelf (Figure 6b).

We interpret the vertical low-velocity zones at the inner shelf as taliks (Figure 6b) that incise into the extensive to intermediate discontinuous IBoPF. A major talik is located between 4.5 and 6.2 km along the profile. It is ~1.7 km wide and >300 m deep. In general, the taliks southeast of 5 km distance show smaller depths than the taliks for distances >10 km. This trend of deepened taliks culminates in the plunging top of IBoPF towards the shelf margin.

Well-bonding permafrost can be found close to the seafloor at the inner shelf. In the upper 100 m, a few local well-bonding permafrost patches occur that extend no deeper than 200 m (Figure 6b). At the outer shelf, well-bonding permafrost is only found as an ice lens close to the shelf edge (Figure 6b).

Similarities between the occurrence of IBoPF and SBP data (Figure 6a) can also be observed. While the acoustic penetration of the SBP data is reduced at the inner shelf, where the top of the IBoPF is shallow, the acoustic

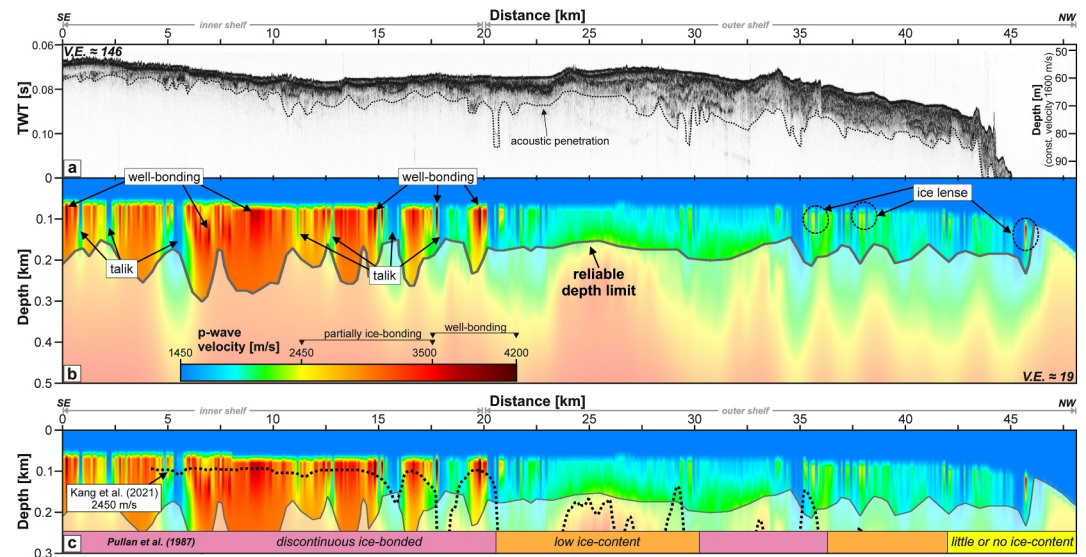


Figure 6. Velocity field indicating ice-bonding permafrost. (a) Shows the co-located SBP data of line 05, (b) the upper 500 m of the velocity field and (c) a comparison with Kang et al. (2021) and Pullan et al. (1987). In (a) the maximum acoustic penetration of the SBP data is displayed as the black dotted line, and in (b) the black solid line shows the maximum depth of reliable velocities. In (c) the black dotted line shows the 2,450 m/s isoline from Kang et al. (2021).

penetration increases towards the shelf edge, where the IBoPF has plunged to >200 m. Where we have identified taliks, the acoustic penetration can be locally increased (e.g., at ~11 and ~21 km, Figure 6a).

The result of the DWT indicates a clear lateral variability of IBoPF between the inner and outer shelf. We interpret the lateral variability of the top of IBoPF as a sign of degraded IBoPF at the outer shelf. At the inner shelf, the top of IBoPF occurs extensively discontinuously as it is dissected by taliks. At the outer ~27 km of the shelf, the top of IBoPF has plunged to at least >200 m depth.

6. Discussion

6.1. Evaluation of the DWT Result

The result of the DWT is critically dependent on the start velocity model (Tanis et al., 2006). In a slower start model, diving waves are expected to penetrate deeper in contrast to a shallower penetration in a faster model. In the extreme, too slow velocities would prevent diving waves to return and too fast velocities would cause an immediate return. To test the effect of the start model and thus, the robustness of the DWT result, a second start model with a higher initial velocity gradient was tested. Its underlying velocity has a water velocity of 1,460 m/s, a seafloor velocity of 1,600 m/s, an increased velocity of 3,800 m/s at 30 mbsf and a velocity of 4,000 m/s for depths ≥ 500 mbsf (Figure 2e).

The DWT result with this faster start model (result 2, Figure 4c) demonstrates an equal IBoPF structure with only minor deviations relative to result 1 (Figures 4c and 4d). Velocities indicating well-bonded permafrost are distributed equally close to the seafloor but are also abundant at greater depth, probably due to the higher maximum velocity allowed in the start model (see Figure 2e). The performance and convergence of the DWT using the faster start model is very similar to the first result with slower start velocities (Figure S1 in Supporting Information S1). The initial and estimated errors as well as the percent change converge to the same values independent of the start model. Only the number of returned rays is constantly higher with the faster start model as expected for diving waves. This is a consequence of the higher start gradient facilitating rays to return to the surface as both the other parameters and the two velocity fields themselves are otherwise very similar.

Having a closer look at Figure 4d, the difference between result 2 and result 1 lies mainly within ± 150 m/s in the upper 300 m. Differences exceeding ± 150 m/s are seen either deeper than 200 m within the first 15 km distance of the line, or show up as localized shallow anomalies. These shallow anomalies often appear as “velocity dipoles”, that is, a high positive difference juxtaposed to a high negative difference (see close-up in Figure 4d). These

“velocity dipoles” are at minimum ~ 100 m wide and ~ 50 m thick and correspond to the same local high velocity patch that is seen just laterally shifted between one inversion result to another (compare to Figures 4b and 4c). Since the shifted high velocities are likely to have the same geological cause (and correspond to clear refracted arrivals in the shot records), we estimate the practical resolution of the DWT to be ~ 100 m laterally and ~ 50 m vertically. The absolute mean velocity errors between the seafloor and the reliable depth limit were also estimated from the difference between the two velocity inversions and is approximately ± 140 m/s.

6.2. Ice-Bearing Permafrost Condition Inferred From Seismic Velocity

Kang et al. (2021) applied a Laplace-domain full-waveform inversion (LFWI) on seismic line ARA05C-05—the same as used here—to image the lower boundary and the internal shape of submarine IBoPF. Both the DWT result and the LFWI result of Kang et al. (2021) show the absence of IBoPF within the upper 200 m at the outer shelf (>20 km distance) and near-surface IBoPF can only be found at the inner shelf (black dotted line, Figure 6c). While the LFWI's top of IBoPF is actually a few tens of meters deeper than in the result from the DWT, the lateral position of the top of IBoPF generally coincides. The location of taliks imaged by both studies mostly coincide as well.

The absence of IBoPF at the outer shelf was also already proposed by Pullan et al. (1987) based on the analysis of paper record of industry seismic data. In Figure 6c, the lateral IBoPF distribution determined by Pullan et al. (1987) is illustrated as colored boxes along the bottom of the profile. This lateral IBoPF distribution can be confirmed by the DWT result (Figure 6c). The transition from discontinuous ice-bonding to low ice content coincides with the descent of the top of IBoPF in the DWT as well as low and little ice content covers most of the outer shelf. However, by applying the DWT, we achieve a better lateral resolution and can add more details to the actual IBoPF zones and distribution proposed by Pullan et al. (1987). We are able to identify where local taliks dissect the zone of discontinuous IBoPF at the inner shelf, and where localized patches of well-bonding permafrost occur in the upper 100 m. This shallow well-bonding permafrost is also observed as ice lenses at the outer shelf.

Missing information about sediment composition or subsurface temperature prevents a quantitative link between P-wave velocity and ice content in the Beaufort Sea (e.g., MacAulay & Hunter, 1982). Consequently, inferring the ice content of the sediments from seismic velocities alone is limited. Therefore, we focus on seismic velocities of $>2,450$ m/s as an indication of IBoPF consistent with previous works in the Canadian and U.S. Beaufort Sea regions (Brothers et al., 2012; Hatlelid & MacDonald, 1982; King et al., 1982; Pullan et al., 1987). This velocity boundary may not represent the entire IBoPF section because lower velocities were used in the past to infer frozen sediments (Brothers et al., 2012; King et al., 1982; Pullan et al., 1987). An underestimation of the general amount of IBoPF is possible. However, the lateral variability of IBoPF between the inner and outer shelf, reflecting the progress of permafrost degradation, would still be observable.

6.3. Degradation of Submarine Ice-Bearing Permafrost

We interpret the absence of IBoPF in the upper strata of the outer shelf to represent the result of permafrost degradation that is ongoing since the marine transgression began in the Holocene (Taylor, 1991). Recent indications that permafrost degradation is ongoing at the shelf edge of the Canadian Beaufort Sea were found by Gwiazda et al. (2018) and Paull et al. (2011, 2022, 2024). Recently, Paull et al. (2022, 2024) observed a rapid change in seafloor morphology at the shelf edge including collapsed seafloor depressions accompanied by volume loss, and formation and collapsing of pingo-like features which they related to submarine groundwater flow. This groundwater may originate from thawed IBoPF at depth (Paull et al., 2024).

Rates of submarine permafrost degradation are known only very locally. For instance, offshore Muostakh Island in the Laptev Sea, Shakhova et al. (2017) present a deepening of the top of IBoPF of ~ 14 cm/year in an area with bottom waters of mean annual temperatures of 0.5°C . In contrast, the Canadian Beaufort Sea exhibits colder bottom waters at the shelf of $\sim -1.5^{\circ}\text{C}$ (Carmack et al., 1989; Jin et al., 2015; Riedel et al., 2015) suggesting a lower degradation rate. Assuming a deepening of ~ 250 m of the top of IBoPF at the outer Canadian Beaufort Shelf (Figure 6), one could speculate a degradation rate in the magnitude of $1\text{--}2$ cm/year for an inundation time of ~ 14 ka in ~ 70 m water depth (Peltier & Fairbanks, 2006).

However, the depth of IBoPF does not depend on inundation time alone (Angelopoulos et al., 2020; Taylor et al., 1996). At the Canadian Beaufort Shelf, for example, the top of IBoPF at a drill site 50 km offshore was reported at 50 mbsf being inundated for 6,000 years (~ 0.8 cm/year at the well Amauligak) whereas the top of IBoPF at a drill site 12 km offshore was reported at 88 mbsf that became inundated 3,500–4,000 years ago (~ 22 –25 cm/year at well 90GSCBH2) (Taylor et al., 1996). Taylor et al. (1996) therefore suggested that thermokarst lakes with taliks may have existed before inundation which could have caused a deeper thawing of areas that were inundated later. Such scales in the order of decimeters per year for degradation rates of submarine IBPF cannot be resolved by repeated seismic surveys with the methodology presented here. Other factors that play a role in permafrost degradation are the thermal conductivity of the geological media, the geothermal gradient and its variance and focused heat transfer from deeper geological structures (e.g., permeable faults) (Angelopoulos et al., 2019; Hinz et al., 1998; Paull et al., 2007).

At the Canadian Beaufort Shelf, in the presence of negative bottom water temperatures with a salinity between 32 and 33 psu (Carmack et al., 1989), intrusions of saline oceanic water could enhance the ongoing degradation of IBoPF. Salinities from sediment samples 7–81 m deep along the Beaufort Shelf were investigated by King et al. (1982) and are in the range of ~ 1 –17 psu. Saline intrusion will transport salt into the sediments via diffusion or gravity-driven pore fluid convection depressing the freezing point of the pore water. The salt transport mechanism is sensitive to the sediment type where diffusion dominates in fine-grained sediments and pore fluid convection dominates in coarse-grained sediments (Osterkamp, 2001). The extent of submarine IBPF may thus be controlled by the combination of the saline input and the submarine groundwater outflow in the shelf edge area that influences the saltwater-freshwater transition (Angelopoulos & Paull, 2024; Frederick & Buffett, 2015). Evidence for far-reaching and widespread groundwater flow across the study region was recently found by gravity coring (Gwiazda et al., 2018) and ROV diving at the slope (Paull et al., 2021).

6.4. Using DWT in Depth Migration

One of the immediate questions that arises is how the DWT velocities may help improve seismic processing and depth imaging in submarine IBPF environments. The DWT provides the high-resolution velocity field of the upper few hundred meters where seismic reflection data suffer from high-energy free-surface multiples making a precise NMO velocity analysis usually unfeasible in the upper ~ 0.5 s TWT or even deeper. Those high-energy free-surface multiples are generated not only at the seafloor but also by the high impedance contrast between the thin veneer of unconsolidated sediments and the top of IBPF (Duchesne et al., 2022). Our data face additional challenges due to the large offset between the source and the nearest receiver, resulting in a limited number of traces capturing reflected energy. Combined with high shallow subsurface velocity contrasts, these factors result in significant NMO stretch effects, severely constraining reliable NMO velocity analysis for shallow reflections.

We performed a Kirchhoff prestack depth migration (PSDM) using the DWT velocity field merged with a velocity field from an NMO velocity and common image gather (CIG) analysis. The shallowest reliable velocity pick below the seafloor in the NMO/CIG-analysis is at ~ 0.5 km depth along the shelf portion of the profile. The shallow DWT velocities were merged with the deeper NMO/CIG velocities along the reliable depth horizon in Figure 6 to get a complete velocity field along the profile (Figure 7a). As the maximum depth of the DWT velocity field and the shallowest NMO pick do not coincide, the velocity field in this gap falls back onto the velocity gradient between seafloor and shallowest NMO pick. It should be noted that we did not observe any reflection from the base of IBPF along this line. All processing steps that were used to prepare and perform the PSDM are shown in Figure S3b in Supporting Information S1.

When performing the PSDM, we encountered issues with the imaging using the merged velocities as shown in Figure 7a.

6.5. Permafrost Induced Anisotropy

Using these interval velocities for the PSDM makes the resulting image geologically unrealistic. A possible reason could be that the seismic waves have experienced different velocities depending on the direction of wave propagation. While diving and refracted waves propagate mainly in a horizontal direction, reflected waves propagate mainly vertically. To account for this physical difference, we assume an anisotropy for the DWT velocities, for example, a vertical transverse isotropy (VTI) which compensates for the velocity difference for different propagation directions. The anisotropy is expressed by two parameters ϵ and δ , in which we assume

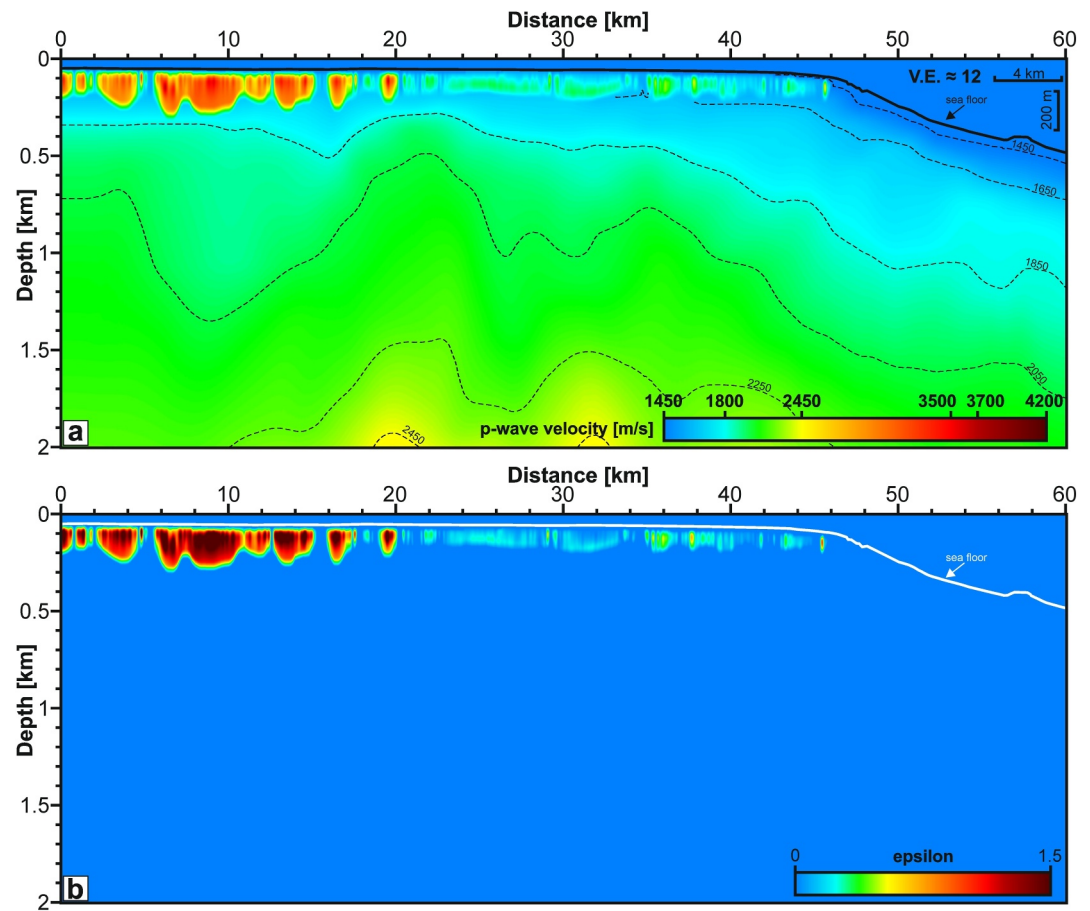


Figure 7. Combined interval velocity field that consists of the DWT result in the near-surface and beneath the result of an NMO/CIG velocity analysis (a). Only velocities from the DWT above the reliable depth limit were used. Used anisotropy parameter ϵ is shown in (b).

$\epsilon > \delta = 0$ for the VTI. Parameter ϵ is estimated as $\epsilon = \frac{1}{2} \left[\left(\frac{v_h}{v_v} \right)^2 - 1 \right]$ from the ratio of the horizontal velocity v_h from the DWT and the vertical velocity v_v from the NMO/CIG velocity analysis (Figure 7b) (Thomsen, 1986).

Figure 8 shows the upper 2 km of the seismic line after PSDM using anisotropic interval velocities (see entire section in Figure S4 in Supporting Information S1). Figures 8a and 8b compare the seismic section when using anisotropic or isotropic (direction-independent) interval velocities (see Figure S5 in Supporting Information S1 for a side-by-side comparison). In Figure 8a, the shallow subsurface is highly distorted after the PSDM when only isotropic velocities are used. Even reflections in the deeper subsurface are affected as they vanish or are destroyed (Figure 8b). This is not the case when anisotropic velocities are used.

For comparison, an anisotropic PSDM was also applied to seismic data in a permafrost environment at the Taglu Gas Field, Mackenzie River Delta, ~100 km south of our study area (Mah et al., 2006). In their work, the authors also had to compensate for different horizontal and vertical P-wave velocities to increase the structural correctness of the seismic depth section. Anisotropy is also not limited to acoustic wave propagation. Sherman and Constable (2018) found anisotropy in submarine IBPF using electrical resistivity data from the Alaskan Beaufort Shelf. Their results also suggested a transverse isotropy.

A VTI may arise simply from the fact that the diving waves basically travel along the horizontally layered IBPF layers (Figure 2a) experiencing a high fraction of ice-related high velocities. In contrast, reflected waves “only” cross these high-velocity layers experiencing a smaller fraction of higher velocities. This could cause a VTI only from the distinctive difference in geometric propagation of the waves. However, we only assume and approximate a VTI and its parameters, so that we obtain a geologically reasonable image. We do not further investigate the

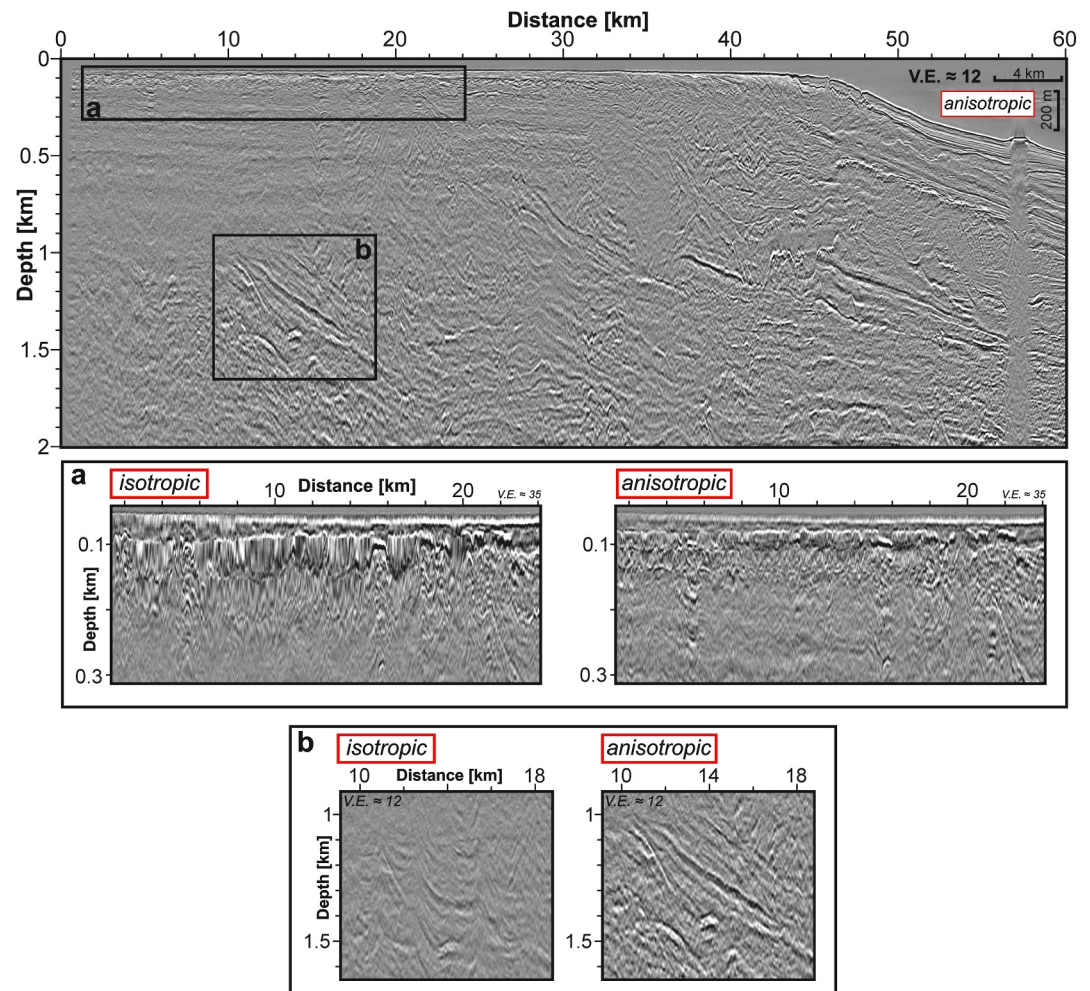


Figure 8. Kirchhoff prestack depth migrated seismic (PSDM) section of line ARA05C-05. Details (a) and (b) show the significant differences when considering isotropic or anisotropic velocities (Figure 7b, $\epsilon > \delta = 0$ (Thomsen, 1986)) for the migration. A side-by-side comparison is shown in Figure S5 in Supporting Information S1.

anisotropy here, but it shows the complexity of the relationship between ice and seismic velocity. It increases the uncertainty in quantifying ice in IBPF by seismic methods without indispensable in-situ information on geological and physical properties of the subsurface.

7. Conclusions

Submarine IBPF occurrences in shallow Arctic continental shelves state a complex environment for subsurface imaging. High-velocity contrasts as well as variable velocity distributions of IBPF are suited for the application of a diving wave tomography. Therefore, this method is applied to a seismic line crossing the outer ~50 km of the Canadian Beaufort Shelf and provides a seismic velocity field for the upper 200–300 mbsl. Although detailed information about the geological and physical properties of the subsurface is missing in the study area, we can infer IBPF conditions from seismic velocities and get a high-resolution insight into the present structure of IBPF.

The result indicates a clear difference in the occurrence of IBPF between the inner and outer Canadian Beaufort Shelf. At the inner shelf, IBPF occurs close to the seafloor but is interrupted by taliks. At the outer ~27 km of the shelf, IBPF is absent in the upper sediments and only isolated ice lenses occur. The top of IBPF has plunged here to >200 mbsl. We interpret the absence of IBPF in the upper strata as a result of permafrost degradation linked to the marine transgression since the Holocene. While present bottom water temperatures are ~−1.5°C, ongoing IBPF degradation could be caused by the intrusion of saline oceanic water.

In addition, the velocity field of the diving wave tomography allows the application of a prestack depth migration which gave best results assuming a VTI anisotropy within the submarine IBPF. The anisotropy adds to the complexity of the relationship between ice and seismic velocity and increases the uncertainty in quantifying ice in IBPF without in-situ information on geological and physical properties of the subsurface.

Data Availability Statement

The seismic data used in this study and the velocity models are available at <https://dx.doi.org/doi:10.22663/KOPRI-KPDC-00002502.2> (Jin et al., 2024).

Acknowledgments

This study is funded by the German Research Foundation (DFG Grant Number KR2222/27-1, RI2107/3-1) and by the Korea Ministry of Oceans and Fisheries (KIMST, 20210632). This work benefited from the support of the Environmental Geoscience Program of the Geological Survey of Canada (GSC) and is part of an ongoing international collaboration between the GSC, Monterey Bay Aquarium Research Institute, KOPRI and several university partners in Canada and Germany to assess the geohazard potential and environmental impacts of permafrost degradation in the Canadian Beaufort Sea. We further like to acknowledge the crew and scientific staff of the IBRV ARAON during expedition ARA05C. We would like to thank Schlumberger for providing the VISTA Desktop Seismic Data Processing software (Version 2020), S&P Global for the Kingdom software (Version 2021) and ESRI for ArcGIS 10.6 under Academic User License Agreements. Open Access funding enabled and organized by Projekt DEAL.

References

- Abdul Basit, A. S., Md Arshad, A. R., & Permalu, A. (2022). Diving wave tomography: Velocity modelling using first arrival traveltimes. *Bulletin Geological Society of Malaysia*, 73(1), 13–22. <https://doi.org/10.7186/bgs73202202>
- Angelopoulos, M., Overduin, P. P., Miesner, F., Grigoriev, M. N., & Vasiliev, A. (2020). Recent advances in the study of Arctic submarine permafrost. *Permafrost and Periglacial Processes*, 31(3), 442–453. <https://doi.org/10.1002/ppp.2061>
- Angelopoulos, M., & Paull, C. K. (2024). Subarctic permafrost formation around seafloor seeps. *Nature Geoscience*, 17(10), 956–957. <https://doi.org/10.1038/s41561-024-01549-4>
- Angelopoulos, M., Westermann, S., Overduin, P., Faguet, A., Olenchenko, V., Grosse, G., & Grigoriev, M. N. (2019). Heat and salt flow in subsea permafrost modeled with CryoGRID2. *Journal of Geophysical Research: Earth Surface*, 124(4), 920–937. <https://doi.org/10.1029/2018JF004823>
- Blasco, S. M., Bennett, R., Brent, T. A., Burton, M., Campbell, P., Carr, E., et al. (2013). 2010 state of knowledge: Beaufort Sea seabed geohazards associated with offshore hydrocarbon development. *Geological Survey of Canada Open File Report*, 6989, 1–340. <https://doi.org/10.4095/292616>
- Brigham, J. K., & Miller, G. H. (1983). Paleotemperature estimates of the alaskan arctic coastal plain during the last 125,000 years. *Permafrost - Fourth International Conference*, 80–85.
- Brothers, L. L., Hart, P. E., & Ruppel, C. D. (2012). Minimum distribution of subsea ice-bearing permafrost on the U. S. Beaufort Sea continental shelf. *Geophysical Research Letters*, 39(June), 1–6. <https://doi.org/10.1029/2012GL052222>
- Brothers, L. L., Herman, B. M., Hart, P. E., & Ruppel, C. D. (2016). Subsea ice-bearing permafrost on the U.S. Beaufort margin: 1. Minimum seaward extent defined from multichannel seismic reflection data. *Geochemistry, Geophysics, Geosystems*, 17(11), 4354–4365. <https://doi.org/10.1002/2016GC006584>
- Brouckov, A. (2003). Frozen saline soils of the Arctic coast: Their distribution and engineering properties. In *Proceedings of the 8th International Conference on Permafrost* (pp. 95–100).
- Carmack, E. C., Macdonald, R. W., & Papadakis, J. E. (1989). Water mass structure and boundaries in the Mackenzie shelf estuary. *Journal of Geophysical Research*, 94(C12), 18043–18055. <https://doi.org/10.1029/JC094iC12p18043>
- Dallimore, S. R., Paull, C. K., Taylor, A. E., Riedel, M., MacAulay, H. A., Côté, M. M., & Jin, Y. K. (2015). Geohazard investigations of permafrost and gas hydrates in the outer shelf and upper slope of the Canadian Beaufort Sea. In *Proceedings of a Symposium to Commemorate the Contributions of J. Ross Mackay (1915–2014) to Permafrost Science in Canada, 7th Canadian Permafrost Conference* (pp. 37–42).
- Dixon, J. (1996). Geological atlas of the Beaufort-Mackenzie area. *Natural Resources Canada*, 173. <https://doi.org/10.4095/207658>
- Dixon, J., & Dietrich, J. R. (1990). Canadian Beaufort Sea and adjacent land areas. In A. Grantz, L. Johnson, & J. F. Sweeney (Eds.), *The Arctic Ocean Region* (Vol. L, pp. 239–256). Geological Society of America. <https://doi.org/10.1130/dnag-gna-1.239>
- Dixon, J., Dietrich, J. R., & McNeil, D. H. (1992). Upper cretaceous to Pleistocene sequence stratigraphy of the beaufort-mackenzie and banks Island areas, northwest Canada. In *Geological Survey of Canada, bulletin*. Geological Survey of Canada. <https://doi.org/10.4095/133237.100>
- Dobinski, W. (2011). Permafrost. *Earth-Science Reviews*, 108(3–4), 158–169. <https://doi.org/10.1016/j.earscirev.2011.06.007>
- Dou, S., Nakagawa, S., Dreger, D., & Ajo-Franklin, J. (2016). A rock-physics investigation of unconsolidated saline permafrost: P-wave properties from laboratory ultrasonic measurements. *Geophysics*, 81(1), WA233–WA245. <https://doi.org/10.1190/geo2015-0176.1>
- Duchesne, M. J., Fabien-Ouellet, G., & Bustamante, J. (2022). Detecting subsea permafrost layers on marine seismic data: An appraisal from forward modelling. *Near Surface Geophysics*, 21(1), 3–20. <https://doi.org/10.1002/nsg.12231>
- Frederick, J. M., & Buffett, B. A. (2015). Effects of submarine groundwater discharge on the present-day extent of relict submarine permafrost and gas hydrate stability on the Beaufort Sea continental shelf. *Journal of Geophysical Research: Earth Surface*, 120(3), 417–432. <https://doi.org/10.1002/2014JF003349>
- Grob, H., Riedel, M., Duchesne, M. J., Krastel, S., Bustamante, J., Fabien-Ouellet, G., et al. (2023). Revealing the extent of submarine permafrost and gas hydrates in the Canadian arctic Beaufort Sea using seismic reflection indicators. *Geochemistry, Geophysics, Geosystems*, 24(5), 1–22. <https://doi.org/10.1029/2023GC010884>
- Gviavza, R., Paull, C. K., Dallimore, S. R., Melling, H., Jin, Y. K., Hong, J. K., et al. (2018). Freshwater seepage into sediments of the shelf, shelf edge, and continental slope of the Canadian Beaufort Sea. *Geochemistry, Geophysics, Geosystems*, 19(9), 3039–3055. <https://doi.org/10.1029/2018GC007623>
- Hatlelid, W. G., & MacDonald, J. R. (1982). Permafrost determination by seismic velocity analyses. *Journal of the Canadian Society of Exploration Geophysicists*, 18(1), 14–22.
- Hinz, K., Delisle, G., & Block, M. (1998). Seismic evidence for the depth extent of permafrost in shelf sediments of the Laptev Sea, Russian Arctic? *PERMAFROST - Seventh International Conference*, 55, 453–457.
- Hivon, E. G., & Sego, D. C. (1993). Distribution of saline permafrost in the Northwest Territories, Canada. *Canadian Geotechnical Journal*, 30(3), 506–514. <https://doi.org/10.1139/t93-043>
- Hu, K., Issler, D. R., Chen, Z., & Brent, T. A. (2013). Permafrost investigation by well logs, and seismic velocity and repeated shallow temperature surveys, Beaufort-Mackenzie Basin. In *Geological Survey of Canada Open File Report*. <https://doi.org/10.4095/293120.33>
- Hunter, J. A., Neave, K. G., MacAulay, H. A., & Hobson, G. D. (1978). Interpretation of sub-seabottom permafrost in the Beaufort Sea by seismic methods: Part 1: Seismic refraction methods. In *Proceedings of the 3rd International Permafrost Conference* (Vol. 515, 520).
- Jakobsson, M., Mayer, L. A., Bringenspar, C., Castro, C. F., Mohammad, R., Johnson, P., et al. (2020). The international bathymetric Chart of the Arctic Ocean version 4.0. *Scientific Data*, 7(1), 1–14. <https://doi.org/10.1038/s41597-020-0520-9>

- Jin, Y. K., & Dallimore, S. R. (2016). ARA05C marine research expedition Canada-Korea-USA Beaufort Sea geoscience research Program: Summary of 2014 activities. *Geological Survey of Canada, Open File*, 7999. <https://doi.org/10.4095/297866>
- Jin, Y. K., Kang, S.-G., Hong, J., & Grob, H. (2024). Seismic data (ARA05C-05) and related velocity models for investigation of the near-surface submarine permafrost conditions in the Canadian Beaufort Sea using diving wave tomography [Dataset]. *Korea Polar Research Institute*. <https://doi.org/10.22663/KOPRI-KPDC-00002502.2>
- Jin, Y. K., Riedel, M., Hong, J. K., Nam, S. I., Jung, J. Y., Ha, S. Y., et al. (2015). Overview of field operations during a 2013 research expedition to the southern Beaufort Sea on the RV Araon. *Geological Survey of Canada, Open File*, 7754. <https://doi.org/10.4095/295856>
- Johansen, T. A., Digraanes, P., van Schaack, M., & Lønne, I. (2003). Seismic mapping and modeling of near-surface sediments in polar areas. *Geophysics*, 68(2), 566–573. <https://doi.org/10.1190/1.1567226>
- Kang, S.-G., Jin, Y. K., Jang, U., Duchesne, M. J., Shin, C., Kim, S., et al. (2021). Imaging the P-wave velocity structure of arctic subsea permafrost using laplace-domain full-waveform inversion. *Journal of Geophysical Research: Earth Surface*, 126(3), 1–15. <https://doi.org/10.1029/2020JF005941>
- Kearey, P., Brooks, M., & Hill, I. (2002). *An Introduction to Geophysical Exploration*. Wiley-Blackwell.
- King, M. S., Pandit, B. I., Hunter, J. A., & Gajtani, M. (1982). Some seismic, electrical, and thermal properties of sub-seabottom permafrost from the Beaufort Sea. In *Proceedings 4th Canadian Permafrost Conference* (pp. 268–273).
- King, M. S., Zimmerman, R. W., & Corwin, R. F. (1988). Seismic and electrical properties of unconsolidated permafrost. *Geophysical Prospecting*, 36(4), 349–364. <https://doi.org/10.1111/j.1365-2478.1988.tb02168.x>
- Lewis, K. A., & Collett, T. S. (2013). *Brookian Sequence Well Log Correlation Sections and Occurrence of Gas Hydrates, North-Central North Slope* (Vol. 2013–5050). U.S. Geological Survey Scientific Investigations Report.23.
- MacAulay, H. A., & Hunter, J. A. (1982). Detailed seismic refraction analysis of ice-bonded permafrost layering in the Canadian Beaufort Sea. In *Proceedings 4th Canadian Permafrost Conference* (pp. 256–267).
- Mah, M., Cheadle, S., Reed, G., & Chang, P. (2006). *Imaging Taglu: Anisotropic PSDM in a permafrost environment* (Vol. 2006, pp. 2392–2395). SEG Technical Program Expanded Abstracts. <https://doi.org/10.1190/1.2370015>
- Matson, R., Wolf, K., & Yancey, D. (2013). Influence of permafrost on seismic imaging in Alaska. *Society of Petroleum Engineers - SPE Arctic and Extreme Environments Conference and Exhibition, AEE 2013*, 1(October), 76–102. <https://doi.org/10.2118/166821-ms>
- Matsushima, J., Suzuki, M., Kato, Y., & Rokugawa, S. (2016). Ultrasonic measurements of attenuation and velocity of compressional and shear waves in partially frozen unconsolidated sediment and synthetic porous rock. *Geophysics*, 81(2), D141–D153. <https://doi.org/10.1190/geo2015-0350.1>
- McLaughlin, F. A., Carmack, E. C., Macdonald, R. W., Melling, H., Swift, J. H., Wheeler, P. A., et al. (2004). The joint roles of Pacific and Atlantic-origin waters in the Canada Basin, 1997–1998. *Deep Sea Research Part I: Oceanographic Research Papers*, 51(1), 107–128. <https://doi.org/10.1016/j.dsr.2003.09.010>
- Natali, S. M., Holdren, J. P., Rogers, B. M., Treharne, R., Duffy, P. B., Pomerance, R., & MacDonald, E. (2021). Permafrost carbon feedbacks threaten global climate goals. *Proceedings of the National Academy of Sciences*, 118(21), e2100163118. <https://doi.org/10.1073/pnas.2100163118>
- O'Connor, M. J., Blasco, S. M., & Pelletier, B. R. (1987). Subsea acoustically defined permafrost (APF types). In *Marine Science Atlas of the Beaufort Sea: Geology and Geophysics*. Geological Survey of Canada. <https://doi.org/10.4095/126965.35>
- Osterkamp, T. E. (2001). Sub-sea permafrost. In *Encyclopedia of ocean Sciences* (Vol. 2, pp. 2902–2912). Elsevier. <https://doi.org/10.1006/rwos.2001.0008>
- Overduin, P. P., Haberland, C., Ryberg, T., Kneier, F., Jacobi, T., Grigoriev, M. N., & Ohrnberger, M. (2015). Submarine permafrost depth from ambient seismic noise. *Geophysical Research Letters*, 42, 7581–7588. <https://doi.org/10.1002/2015GL065409>. Received
- Overduin, P. P., Schneider von Deimling, T., Miesner, F., Grigoriev, M. N., Ruppel, C. D., Vasiliev, A., et al. (2019). Submarine permafrost map in the arctic modeled using 1-D transient heat flux (SuPerMAP). *Journal of Geophysical Research: Oceans*, 124(6), 3490–3507. <https://doi.org/10.1029/2018JC014675>
- Paige, C. C., & Saunders, M. A. (1982). Algorithm 583: Lsqqr: Sparse Linear equations and least squares problems. *ACM Transactions on Mathematical Software*, 8(2), 195–209. <https://doi.org/10.1145/355993.356000>
- Paull, C. K., Dallimore, S. R., Caress, D. W., Gwiazda, R., Lundsten, E., & Anderson, K., et al. (2021). A 100-km wide slump along the upper slope of the Canadian Arctic was likely preconditioned for failure by brackish pore water flushing. *Marine Geology*, 435, 106453. <https://doi.org/10.1016/j.margeo.2021.106453>
- Paull, C. K., Dallimore, S. R., Hughes-Clarke, J., Blasco, S. M., Lundsten, E., Ussler, W., et al. (2011). Tracking the Decomposition of Submarine Permafrost and Gas Hydrate under the Shelf and Slope of the Beaufort Sea (pp. 1–12).
- Paull, C. K., Dallimore, S. R., Jin, Y. K., Caress, D. W., Lundsten, E., Gwiazda, R., et al. (2022). Rapid seafloor changes associated with the degradation of Arctic submarine permafrost. In *Proceedings of the National Academy of Sciences* (Vol. 119(12), pp. 1–8). <https://doi.org/10.1073/pnas.2119105119>
- Paull, C. K., Hong, J. K., Caress, D. W., Gwiazda, R., Kim, J.-H., Lundsten, E., et al. (2024). Massive ice outcrops and thermokarst along the arctic shelf edge: By-products of ongoing groundwater freezing and thawing in the sub-surface. *Journal of Geophysical Research: Earth Surface*, 129(10), e2024JF007719. <https://doi.org/10.1029/2024JF007719>
- Paull, C. K., Ussler, W., Dallimore, S. R., Blasco, S. M., Lorenson, T. D., Melling, H., et al. (2007). Origin of pingo-like features on the Beaufort Sea shelf and their possible relationship to decomposing methane gas hydrates. *Geophysical Research Letters*, 34(1), 1–5. <https://doi.org/10.1029/2006GL027977>
- Pelletier, B. R., & Medioli, B. E. (2014). Environmental atlas of the Beaufort coastlands. In *Geological Survey of Canada, Open File* (Vol. 7619, pp. 1–271). <https://doi.org/10.4095/294601>
- Peltier, W. R., & Fairbanks, R. G. (2006). Global glacial ice volume and Last Glacial Maximum duration from an extended Barbados sea level record. *Quaternary Science Reviews*, 25(23–24), 3322–3337. <https://doi.org/10.1016/j.quascirev.2006.04.010>
- Podvin, P., & Lecomte, I. (1991). Finite difference computation of traveltimes in very contrasted velocity models: A massively parallel approach and its associated tools. *Geophysical Journal International*, 105(1), 271–284. <https://doi.org/10.1111/j.1365-246X.1991.tb03461.x>
- Portnov, A., Smith, A. J., Mienert, J., Cherkashov, G., Rekant, P., Semenov, P., et al. (2013). Offshore permafrost decay and massive seabed methane escape in water depths >20 m at the South Kara Sea shelf. *Geophysical Research Letters*, 40(15), 3962–3967. <https://doi.org/10.1002/grl.50735>
- Pullan, S., MacAulay, H. A., Hunter, J. A. M., Good, R. L., Gagne, R. M., Burns, R. A., & Pelletier, B. R. (1987). Permafrost distribution determined from seismic refraction. In *Marine Science Atlas of the Beaufort Sea: Geology and Geophysics*. Geological Survey of Canada. <https://doi.org/10.4095/126967.37>

- Ramachandran, K., Bellefleur, G., Brent, T., Riedel, M., & Dallimore, S. R. (2011). Imaging permafrost velocity structure using high resolution 3D seismic tomography. *Geophysics*, 76(5), B187–B198. <https://doi.org/10.1190/geo2010-0353.1>
- Rekant, P., Bauch, H. A., Schwenk, T., Portnov, A., Gusev, E., Spiess, V., et al. (2015). Evolution of subsea permafrost landscapes in arctic Siberia since the late Pleistocene: A synoptic insight from acoustic data of the Laptev Sea. *Arktos*, 1(1), 11. <https://doi.org/10.1007/s41063-015-0011-y>
- Riedel, M., Brent, T. A., Taylor, G., Taylor, A. E., Hong, J.-K., Jin, Y.-K., & Dallimore, S. R. (2017). Evidence for gas hydrate occurrences in the Canadian Arctic Beaufort Sea within permafrost-associated shelf and deep-water marine environments. *Marine and Petroleum Geology*, 81, 66–78. <https://doi.org/10.1016/j.marpetgeo.2016.12.027>
- Riedel, M., Villinger, H., Asshoff, K., Kaul, N., & Dallimore, S. R. (2015). Temperature measurements and thermal gradient estimates on the slope and shelf-edge region of the Beaufort Sea. *Geological Survey of Canada, Open File*, 7725. <https://doi.org/10.4095/296570>
- Ruppel, C. D., & Kessler, J. D. (2017). The interaction of climate change and methane hydrates. *Reviews of Geophysics*, 55(1), 126–168. <https://doi.org/10.1002/2016RG000534>
- Schindler, M., Batzle, M. L., & Prasad, M. (2016). Micro X-Ray computed tomography imaging and ultrasonic velocity measurements in tetrahydrofuran-hydrate-bearing sediments. *Geophysical Prospecting*, 65(4), 1025–1036. <https://doi.org/10.1111/1365-2478.12449>
- Schuur, E. A. G., Abbott, B. W., Commann, R., Ernakovich, J., Euskirchen, E., Hugelius, G., et al. (2022). Permafrost and climate change: Carbon Cycle feedbacks from the warming arctic. *Annual Review of Environment and Resources*, 47(1), 343–371. <https://doi.org/10.1146/annurev-environ-012220-011847>
- Schuur, E. A. G., McGuire, A. D., Schädel, C., Grosse, G., Harden, J. W., Hayes, D. J., et al. (2015). Climate change and the permafrost carbon feedback. *Nature*, 520(7546), 171–179. <https://doi.org/10.1038/nature14338>
- Shakhova, N., Semiletov, I., Gustafsson, O., Sergienko, V., Lobkovsky, L., Dudarev, O., et al. (2017). Current rates and mechanisms of subsea permafrost degradation in the East Siberian Arctic Shelf. *Nature Communications*, 8(1), 15872. <https://doi.org/10.1038/ncomms15872>
- Sherman, D., & Constable, S. C. (2018). Permafrost extent on the Alaskan Beaufort shelf from surface-towed controlled-source electromagnetic surveys. *Journal of Geophysical Research: Solid Earth*, 123(9), 7253–7265. <https://doi.org/10.1029/2018JB015859>
- Sherman, D., Kannberg, P., & Constable, S. (2017). Surface towed electromagnetic system for mapping of subsea Arctic permafrost. *Earth and Planetary Science Letters*, 460, 97–104. <https://doi.org/10.1016/j.epsl.2016.12.002>
- Stefani, J. P. (1995). Turning-ray tomography. *Geophysics*, 60(6), 1917–1929. <https://doi.org/10.1190/1.1443923>
- Tanis, M. C., Shah, H., Watson, P. A., Harrison, M., Exploration, B. P., Yang, S., et al. (2006). *Diving-wave refraction tomography and reflection tomography for velocity model building* (pp. 3340–3344). SEG Technical Program Expanded Abstracts.
- Taylor, A. E. (1991). Marine transgression, shoreline emergence: Evidence in seabed and terrestrial ground temperatures of changing relative sea levels, Arctic Canada. *Journal of Geophysical Research*, 96(B4), 6893–6909. <https://doi.org/10.1029/91JB00293>
- Taylor, A. E., Dallimore, S. R., Hill, P. R., Issler, D. R., Blasco, S. M., & Wright, F. (2013). Numerical model of the geothermal regime on the Beaufort shelf, arctic Canada since the last interglacial. *Journal of Geophysical Research: Earth Surface*, 118(4), 2365–2379. <https://doi.org/10.1002/2013JF002859>
- Taylor, A. E., Dallimore, S. R., & Outcalt, S. I. (1996). Late Quaternary history of the Mackenzie–Beaufort region, Arctic Canada, from modelling of permafrost temperatures. 1. The onshore–offshore transition. *Canadian Journal of Earth Sciences*, 33(1), 52–61. <https://doi.org/10.1139/e96-006>
- Thomsen, L. (1986). Weak elastic anisotropy. *Geophysics*, 51(10), 1954–1966. <https://doi.org/10.1190/1.1442051>
- van Everdingen, R. O. (1998). Multi-language glossary of permafrost and related ground-ice terms (Rev. Ed. 2005). *International Permafrost Association*, 1998, 159. (revised).
- Wild, B., Shakhova, N., Dudarev, O., Ruban, A., Kosmach, D., Tumskey, V., et al. (2022). Organic matter composition and greenhouse gas production of thawing subsea permafrost in the Laptev Sea. *Nature Communications*, 13(1), 5057. <https://doi.org/10.1038/s41467-022-32696-0>
- Zhu, X., Sixta, D. P., & Angstman, B. G. (1992). Tomostatics: Turning-ray tomography + static corrections. *The Leading Edge*, 11(12), 15–23. <https://doi.org/10.1190/1.1436864>
- Zimmerman, R. W., & King, M. S. (1986). The effect of the extent of freezing on seismic velocities in unconsolidated permafrost. *Geophysics*, 51(6), 1285–1290. <https://doi.org/10.1190/1.1442181>